Article

Molecular Cell

TTC19 Plays a Husbandry Role on UQCRFS1 Turnover in the Biogenesis of Mitochondrial Respiratory Complex III

Graphical Abstract

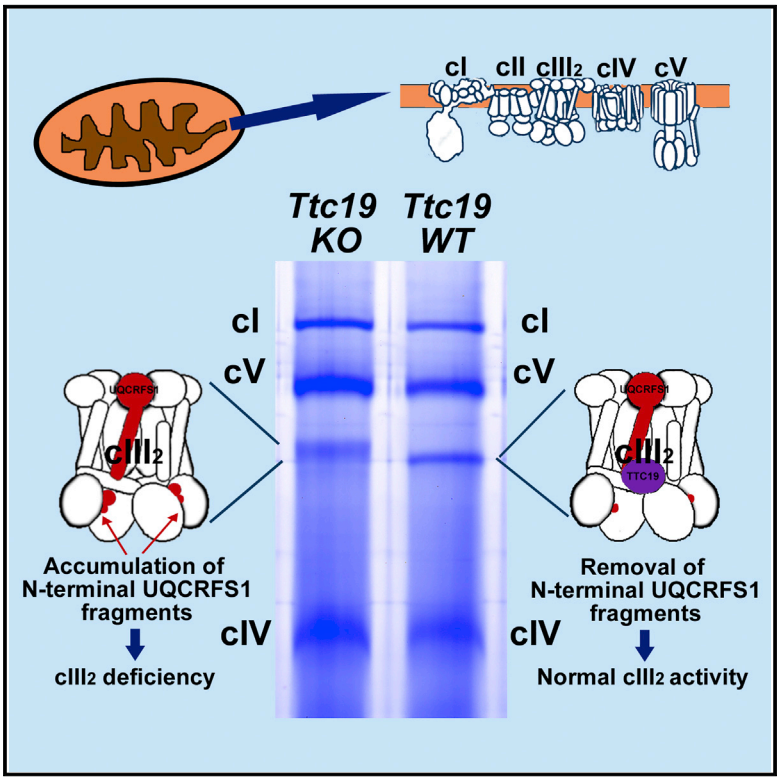

Authors

Emanuela Bottani, Raffaele Cerutti, Michael E. Harbour, ..., Carlo Viscomi, Erika Fernandez-Vizarra, Massimo Zeviani

Correspondence

emfvb2@mrc-mbu.cam.ac.uk (E.F.-V.), mdz21@mrc-mbu.cam.ac.uk (M.Z.)

In Brief

Bottani et al. demonstrate that TTC19, mutated in neurodegeneration associated with complex III deficiency, is involved in the removal of N-terminal proteolytic fragments of the Rieske protein, produced upon incorporation into complex III. Thus, TTC19 allows the physiological turnover of the Rieske protein and the preservation of complex III function.

Highlights

- Absence of TTC19 causes cIII defect and neurological impairment in humans and mice
- TTC19 binds fully assembled cIII, after the incorporation of UQCRFS1
- UQCRFS1 undergoes proteolytic processing after its incorporation in cIII
- TTC19 is involved in the clearance of UQCRFS1 fragments that inhibit cIII

Bottani et al., 2017, Molecular Cell 67, 96–105
July 6, 2017
http://dx.doi.org/10.1016/j.molcel.2017.06.001

CellPress

CellPress

Molecular Cell
Article

TTC19 Plays a Husbandry Role on UQCRFS1 Turnover in the Biogenesis of Mitochondrial Respiratory Complex III

Emanuela Bottani,[1] Raffaele Cerutti,[1] Michael E. Harbour,[1] Sabrina Ravaglia,[2] Sukru Anil Dogan,[1] Carla Giordano,[3] Ian M. Fearnley,[1] Giulia D'Amati,[3] Carlo Viscomi,[1] Erika Fernandez-Vizarra,[1,*] and Massimo Zeviani[1,4,*]
[1]MRC Mitochondrial Biology Unit, University of Cambridge, Wellcome Trust/MRC Building Hills Road, Cambridge CB2 0XY, UK
[2]Istituto Neurologico "Casimiro Mondino," via Mondino 2, Pavia 27100, Italy
[3]Department of Radiological, Oncological and Pathological Sciences, Sapienza University of Rome, 00161 Rome, Italy
[4]Lead Contact
*Correspondence: emfvb2@mrc-mbu.cam.ac.uk (E.F.-V.), mdz21@mrc-mbu.cam.ac.uk (M.Z.)
http://dx.doi.org/10.1016/j.molcel.2017.06.001

SUMMARY

Loss-of-function mutations in *TTC19* (tetra-tricopeptide repeat domain 19) have been associated with severe neurological phenotypes and mitochondrial respiratory chain complex III deficiency. We previously demonstrated the mitochondrial localization of TTC19 and its link with complex III biogenesis. Here we provide detailed insight into the mechanistic role of TTC19, by investigating a *Ttc19*$^{-/-}$ mouse model that shows progressive neurological and metabolic decline, decreased complex III activity, and increased production of reactive oxygen species. By using both the *Ttc19*$^{-/-}$ mouse model and a range of human cell lines, we demonstrate that TTC19 binds to the fully assembled complex III dimer, i.e., after the incorporation of the iron-sulfur Rieske protein (UQCRFS1). The *in situ* maturation of UQCRFS1 produces N-terminal polypeptides, which remain bound to holocomplex III. We show that, in normal conditions, these UQCRFS1 fragments are rapidly removed, but when TTC19 is absent they accumulate within complex III, causing its structural and functional impairment.

INTRODUCTION

Complex III, or ubiquinol:cytochrome *c* oxidoreductase, is the central complex in the mitochondrial electron transport chain. Complex III is a multi-heteromeric enzyme, organized in a symmetrical dimeric structure ($cIII_2$) of ~480 kDa (Iwata et al., 1998). $cIII_2$ catalyzes the transfer of electrons from Coenzyme Q to cytochrome *c*, while pumping protons from the matrix to the intermembrane space. In yeast and birds, the cIII monomer is composed of ten different subunits, whereas an eleventh subunit, Subunit 9 (Su9) in the bovine nomenclature, has been identified in mammals as a post-translational proteolytic product consisting of the 78-amino acid-long N-terminal mitochondrial targeting sequence (MTS) of the 2Fe-2S cluster-containing Rieske protein, encoded by the *UQCRFS1* gene (Brandt et al., 1993). Cytochrome b (MT-CYB), the only $cIII_2$ component encoded by mtDNA, is one of the three catalytic subunits of the complex, and it contains a low-potential (b_L) and a high-potential (b_H) heme b moieties as prosthetic groups. Of the other ten subunits, encoded by nine nuclear genes, two play a catalytic role: the UQCRFS1 Rieske protein and cytochrome *c*1, encoded by *CYC1*, which contains a c-type heme group. The role of the other eight supernumerary subunits remains unclear.

Although $cIII_2$ assembly has been less intensively investigated compared to other respiratory complexes, in the last few years the study of yeast mutant models has provided some insight into this process (Gruschke et al., 2012; Hildenbeutel et al., 2014; Smith et al., 2012; Zara et al., 2009). Studies on $cIII_2$-associated human diseases have confirmed that some $cIII_2$ assembly steps are similar to yeast, especially the late ones. Based on the yeast model, $cIII_2$ assembly starts with the insertion into the inner mitochondrial membrane of MT-CYB, bound to chaperones UQCC1, UQCC2, and UQCC3. These chaperones are released during the sequential incorporation of additional subunits into an inactive dimeric pre-$cIII_2$, which is eventually activated by the incorporation of the last subunits, UQCRFS1 and UQCR11. This final step, i.e., the UQCRFS1 incorporation, is mediated by BCS1L, the most extensively characterized $cIII_2$ assembly factor, and LYRM7 (MZM1L), a matrix protein that stabilizes the subunit before its assembly into $cIII_2$ (Fernández-Vizarra and Zeviani, 2015).

Pathogenic mutations have been found in some of $cIII_2$-related ancillary factors, including BCS1L (de Lonlay et al., 2001; Fellman, 2002; Fernandez-Vizarra et al., 2007; Hinson et al., 2007; Morán et al., 2010; Ramos-Arroyo et al., 2009), TTC19 (Ardissone et al., 2015; Atwal, 2014; Ghezzi et al., 2011; Kunii et al., 2015; Melchionda et al., 2014; Mordaunt et al., 2015; Morino et al., 2014; Nogueira et al., 2013), LYRM7 (Dallabona et al., 2016; Invernizzi et al., 2013), UQCC2 (Tucker et al., 2013), and UQCC3 (Wanschers et al., 2014). In particular, mutations in *TTC19* have been identified in patients with heterogeneous, but invariably severe, phenotypes, including early-onset, slowly progressive encephalomyopathy; adult-onset, rapidly progressive multisystem neurological failure; adult-onset spinocerebellar ataxia; and childhood or juvenile spinocerebellar ataxia with

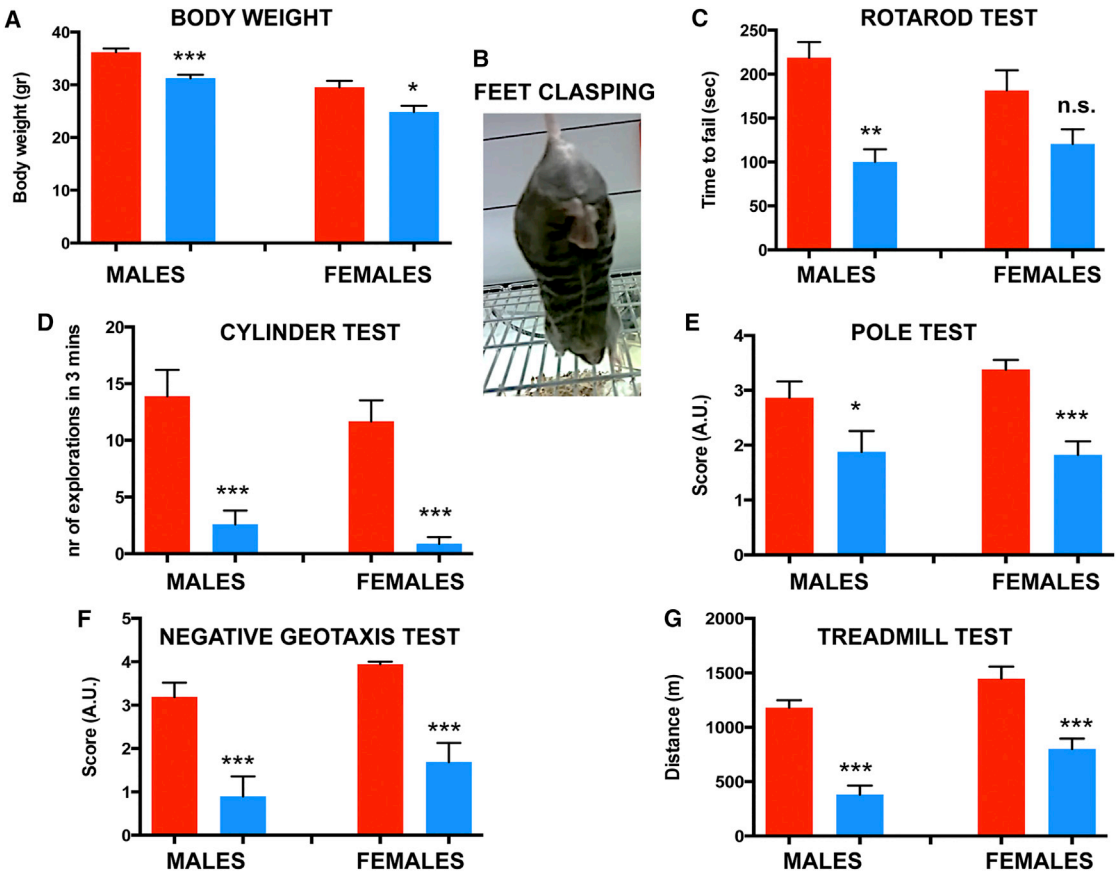

Figure 1. Clinical Characterization of 6-Month-Old *Ttc19*$^{-/-}$ Mice

(A) Body weights of *Ttc19*$^{-/-}$ versus *Ttc19*^{WT} littermates (combined *Ttc19*$^{+/-}$ and *Ttc19*$^{+/+}$ individuals), n = 8–11 animals/group; (B) feet clasping reflex (normal reflex is in abduction, here the lower limbs are tightly adducted), (C) rotarod test, n = 6–8 animals/group, average of three trials/mouse; (D) cylinder test, n = 6–9 animals/group, average of two trials/mouse; (E) pole test, n = 6–9 animals/group, average of five trials/mouse; (F) negative geotaxis test, n = 6–9 animals/group, average of two trials/mouse; and (G) treadmill test, n = 6–11 animals/group. Error bars represent SEM; statistical analysis was by unpaired Student's t test (*p < 0.05, **p < 0.01, and ***p < 0.005; n.s., not significant). Red bars, *Ttc19*^{WT}; blue bars, *Ttc19*$^{-/-}$. See also Figures S2 and S3.

psychosis (OMIM: 613814). *TTC19* encodes the precursor of the tetratricopeptide repeat domain 19 protein. TTC19, a 380-amino acid-long polypeptide, is addressed to mitochondria by a 70-amino acid-long MTS, which is removed after translocation of the protein into the inner mitochondrial compartment. Mature human TTC19 is a 35-kDa protein embedded within the inner mitochondrial membrane, with orthologs in multicellular animals but neither in fungi nor in plants. Unlike other assembly factors, TTC19 binds to mature dimeric $cIII_2$, whereas, in mutant human fibroblasts, its absence leads to the accumulation of lower molecular weight species-containing $cIII_2$ subunits, UQCRC1 and UQCRC2 (Ghezzi et al., 2011). Here we present a study that elucidates the molecular role of TTC19 by investigating human cell and mouse animal models.

RESULTS

Clinical Characterization of Ttc19$^{-/-}$ Mice

We created a constitutive Ttc19$^{-/-}$ mouse by gene targeting (Figure S1). The gender and genotype distribution at birth was compatible with a mendelian autosomal recessive trait and no evidence of embryonic lethality. At 6 months of age, both Ttc19$^{-/-}$ males and females showed a reduction in body weight compared to wild-type (WT) littermates (Figure 1A). No differences were observed between Ttc19$^{+/+}$ and Ttc19$^{+/-}$ animals for any of the parameters investigated; therefore, both genotypes were considered as controls (Ttc19^{WT}). Several tests were used to assess neurological, behavioral, and metabolic features. At 6 months of age, Ttc19$^{-/-}$ mice showed a pathological feet-clasping reflex (Figure 1B), and they scored significantly less than WT littermates in rotarod, cylinder, negative geotaxis, and pole tests, which measure motor coordination, exploratory behavior, general proprioception, and motor planning skills, respectively (Figures 1C–1F). Motor endurance, assessed by standard treadmill test, was also reduced in Ttc19$^{-/-}$ versus Ttc19^{WT} animals (Figure 1G). Some of these features were already present at 3 months of age (Figure S2). No differences in lifespan were observed up to 21 months (data not shown).

To study whole-body metabolism, we used a comprehensive lab animals monitoring system (CLAMS). Ttc19$^{-/-}$ females

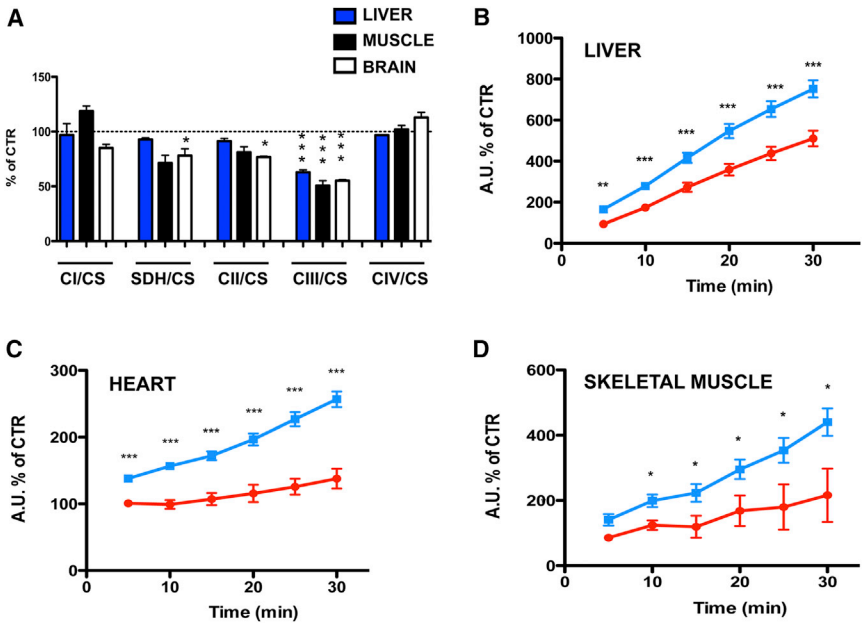

Figure 2. Respiratory Chain Activities and Hydrogen Peroxide Production in *Ttc19*$^{-/-}$ Tissues

(A) Spectrophotometric analysis of biochemical activities of mitochondrial respiratory chain complexes normalized to CS activity and expressed as percentage compared to control values (n = 4 mice/group, age = 3 months old).

(B–D) Time course analysis of H_2O_2 production measured by Amplex Red in isolated mitochondria, without the addition of external substrates or inhibitors, for (B) liver, (C) heart, and (D) skeletal muscle. Error bars represent SEM; statistical analysis was by unpaired Student's t test (*p < 0.05, **p < 0.01, and ***p < 0.005). Blue lines, *Ttc19*$^{-/-}$ samples; red lines, *Ttc19*^{WT} samples; n = 3 animals/group in duplicate.

showed reduced food and water intake compared to Ttc19^{WT} female littermates (Figures S3A and S3B); VO_2 consumption and VCO_2 production were significantly reduced in Ttc19$^{-/-}$ versus Ttc19^{WT} animals of both sexes (Figures S3C and S3D); accordingly, energy expenditure, measured as the ratio between heat rate and body weight, was decreased (Figure S3E), although statistical significance was achieved only in females. Likewise, the respiratory exchange ratio (RER) was significantly reduced in females, suggesting increased utilization of fat versus carbohydrates to produce energy (Figure S3F). Total, ambulatory, and rearing movements were significantly decreased in Ttc19$^{-/-}$ versus Ttc19^{WT} littermates of both genders (Figure S3G). These data indicate neurological impairment and reduction in energy metabolism of Ttc19$^{-/-}$ mice.

Neuropathology of Ttc19$^{-/-}$ Mice

Extensive astrogliosis, most often surrounding dilated vascular structures (Figures S4A and S4C), and the accumulation of ubiquitinated proteins in neurons (Figure S4E) were detected in the thalamus of all *Ttc19*$^{-/-}$ mice analyzed (n = 6), suggesting an ongoing brain injury. These features were not observed in *Ttc19*^{WT} littermates (n = 6) (Figures S4B, S4D, and S4F). No abnormalities were detected in skeletal muscle by H&E (data not shown). Light microscopy of brain sections stained by H&E (data not shown) or Nissl (Figure S4G) did not reveal obvious neuronal loss, compared to *Ttc19*^{WT} brain (Figure S4H). No sign of neurodegeneration or apoptosis was detected by staining brain sections with fluorojade C or terminal deoxynucleotidyl transferase (TdT) dUTP nick-end labeling (TUNEL) (data not shown).

Biochemical Analysis of Ttc19$^{-/-}$ Tissues

Similar to human patients, *Ttc19* ablation in mice caused $cIII_2$ deficiency in all tested tissues. At 3 and 6 months of age, $cIII_2$/citrate synthase (CS) activity was significantly reduced (≈50%, $p < 0.005$) in brain, liver, and skeletal muscle from *Ttc19*$^{-/-}$ versus *Ttc19*^{WT} (Figure 2A), with no gender differences. The residual activity was further reduced (≈40%) at 18 months in both females and males (data not shown). Defective $cIII_2$ activity is associated with increased production of reactive oxygen species (ROS) (Diaz et al., 2012; Hinson et al., 2007), through reverse electron transfer from reduced heme b_L (Borek et al., 2008; Dröse and Brandt, 2008). Accordingly, H_2O_2 production in isolated mitochondria from liver, heart, and skeletal muscle was significantly higher in *Ttc19*$^{-/-}$ compared to *Ttc19*^{WT} littermates (Figures 2B–2D).

Analysis of $cIII_2$ Assembly in Ttc19$^{-/-}$ Tissues

Next, the assembly of $cIII_2$ in mitochondria isolated from mouse brain, liver, and skeletal muscle was investigated by blue native gel electrophoresis (BNGE). First dimension (1D)-BNGE revealed an altered electrophoretic pattern in the *Ttc19*$^{-/-}$ samples from all three tissues (Figure 3A), as the $cIII_2$ band migrated more slowly and appeared blurred. The aberrant band was observed when using either digitonin or dodecyl-maltoside (DDM) as solubilizing detergents (Figure 3B). To further investigate this phenomenon, we carried out complexome profiling of *Ttc19*$^{-/-}$ versus *Ttc19*^{WT} isolated liver (data not shown) and brain mitochondria solubilized with 1% DDM (Figure 3C). The 1D-BNGE lanes were excised in 50 slices, and each slice was analyzed by mass spectrometry. In *Ttc19*$^{-/-}$ mitochondria, $cIII_2$ subunits were detected in an area of the gel slightly wider and with higher apparent molecular mass than $cIII_2$ subunits from *Ttc19*^{WT} mitochondria. Interestingly, a normal migration pattern was restored by adeno-associated virus serotype 2/8 (AAV2/8)-mediated expression of human 6xHis-tagged wild-type TTC19 (hTTC19^{His6}) in *Ttc19*$^{-/-}$ mouse liver mitochondria (Figure S5A), demonstrating that the electrophoretic aberrations were specifically due to the absence of Ttc19.

No accumulation of $cIII_2$ sub-assemblies was detected in mitochondria from *Ttc19*$^{-/-}$ mouse tissues by either complexome profiling (Figure 3C) or denaturing second dimension (2D)-BNGE using antibodies against several subunits of $cIII_2$ (Figure S5B). Proteomic analysis of SDS-PAGE of the native BNGE band corresponding to $cIII_2$ or the immunocaptured $cIII_2$ from *Ttc19*^{WT} in comparison with *Ttc19*$^{-/-}$ failed to show any difference in protein

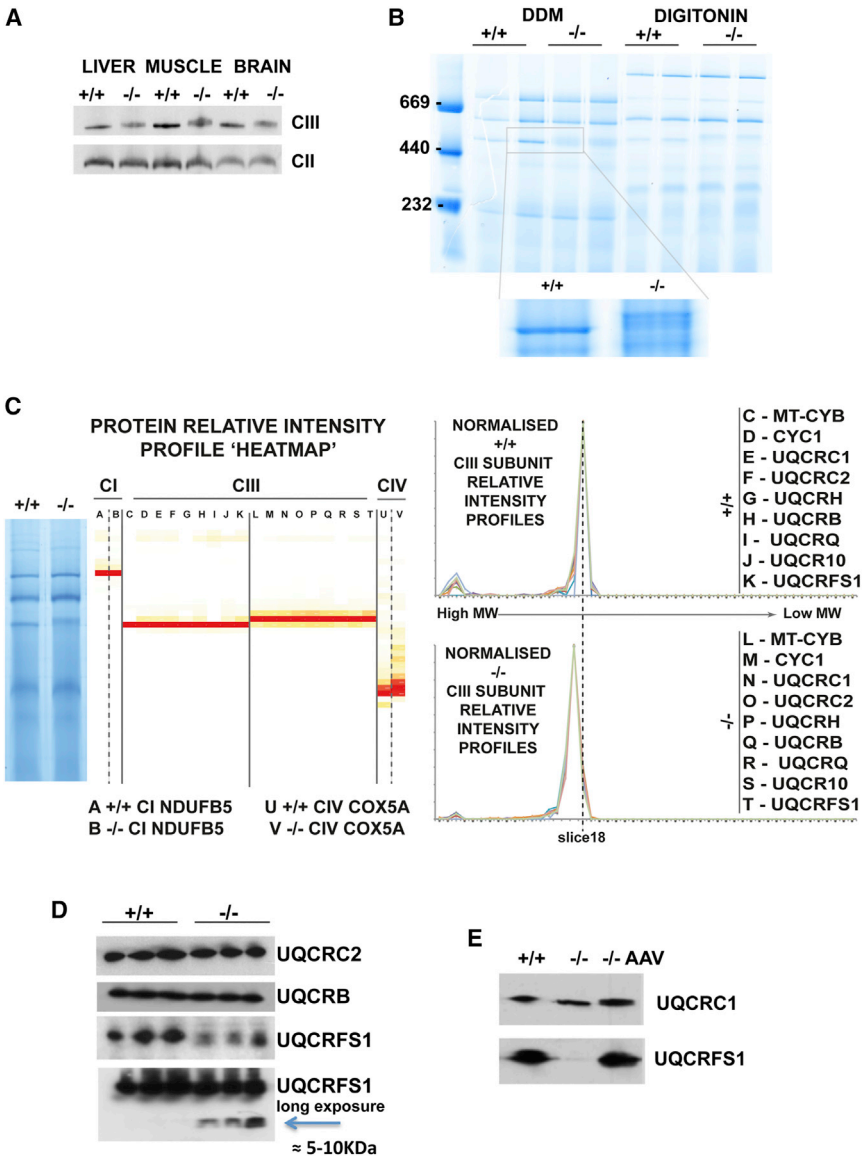

Figure 3. Characterization of $cIII_2$ in *Ttc19*$^{-/-}$ Tissues

(A) Immunovisualization of $cIII_2$ in BNGE of mitochondria extracted from liver, muscle, and brain. Anti-UQCRC1 and anti-SDH70 were used for $cIII_2$ and cII visualization, respectively.

(B) Top: BNGE of *Ttc19*^{WT} and *Ttc19*$^{-/-}$ mitochondria, solubilized with DDM or digitonin. Bottom: an enlargement of the $cIII_2$ band is shown.

(C) Complexome analysis of brain mitochondria solubilized with 1% DDM and run on a 4%–12% BNGE gel cut in 50 slices and individually analyzed by mass spectrometry. Top: heatmap shows the relative peptide intensity among the slices of the indicated subunits. NDUFB5 of complex I and COX5A of complex IV are shown to indicate no differences in their migration. Bottom: profile of the indicated nine complex III subunits is shown. Complex III peak of Ttc19^{WT} localizes in slice 18 whereas that of Ttc19$^{-/-}$ appears at a higher MW.

(D) Western blot (WB) of the subunits in $cIII_2$ bands cut from 1D-BNGE and run on SDS-PAGE.

(E) WB on complex III_2 bands denatured and run on SDS-PAGE. The re-expression of TTC19^{6His} mediated by AAV in the liver of *Ttc19*$^{-/-}$ mice restored the incorporation of intact UQCRFS1 in $cIII_2$.

See also Figure S5.

composition between the two genotypes. However, when the band corresponding to holocomplex $cIII_2$ was isolated and run through a denaturing SDS-PAGE and analyzed by western blot immunodetection, we observed a reduction of incorporated intact UQCRFS1 in *Ttc19*$^{-/-}$ versus *Ttc19*^{WT} mouse samples and the accumulation of UQCRFS1 degradation products (Figure 3D). Interestingly, the levels of intact UQCRFS1 incorporated into $cIII_2$ were restored in *Ttc19*$^{-/-}$ liver (Figure 3E) by expressing hTTC19^{His6} with the AAV2/8-hTTC19^{His6} vector. These results demonstrated a role for TTC19 in stabilizing $cIII_2$, through a specific protective effect on UQCRFS1.

Kinetics of $cIII_2$ Assembly and UQCRFS1 Incorporation in Ttc19$^{-/-}$ Mouse Mitochondria

Next, we investigated the dynamics of incorporation of an early-assembled $cIII_2$ subunit, UQCRB, and of UQCRFS1. The ^{35}S-labeled translation products were incubated with *Ttc19*$^{-/-}$ and *Ttc19*^{WT} mouse liver mitochondria at different times (15-, 30-, and 60-min pulses); samples were then washed and incubated for a further 2 hr (chase). The incorporation into $cIII_2$ of both UQCRB and UQCRFS1 was not significantly different between the *Ttc19*$^{-/-}$ and *Ttc19*^{WT} samples (Figure S6). We then cut the $cIII_2$ band from the BNGE gel and denatured and electrophoresed it by SDS-PAGE. Radiolabeled UQCRFS1-derived fragments, including 12, 8, and 4 kDa in size, were already evident after a 15-min pulse in both *Ttc19*$^{-/-}$ and *Ttc19*^{WT} mitochondria (Figures 4A and 4B). Densitometric analysis of intact UQCRFS1 versus fragmented UQCRFS1 showed that fragmented UQCRFS1 persisted longer in *Ttc19*$^{-/-}$ compared to *Ttc19*^{WT} samples (Figures 4C and 4D). These results indicate that UQCRFS1 is physiologically proteolysed once it is incorporated in $cIII_2$, since fragmented species were bound to $cIII_2$ and present very early in both *Ttc19*$^{-/-}$ and *Ttc19*^{WT} samples, but their clearance was slowed down in *Ttc19*$^{-/-}$ versus *Ttc19*^{WT} mitochondria (Figures 4C and 4D). The percentage of mature, intact UQCRFS1 was lower in *Ttc19*$^{-/-}$ versus *Ttc19*^{WT} at 60 and 180 min, although the difference was not statistically significant ($p = 0.067$) (Figure 4C).

We also analyzed the relative amounts of the UQCRFS1 fragments at different time points. The amount of the 12- and 8-kDa fragments progressively decreased over time, whereas the 4-kDa fragment was virtually unchanged for all the time points of the experiment. However, the decrease in the amount of

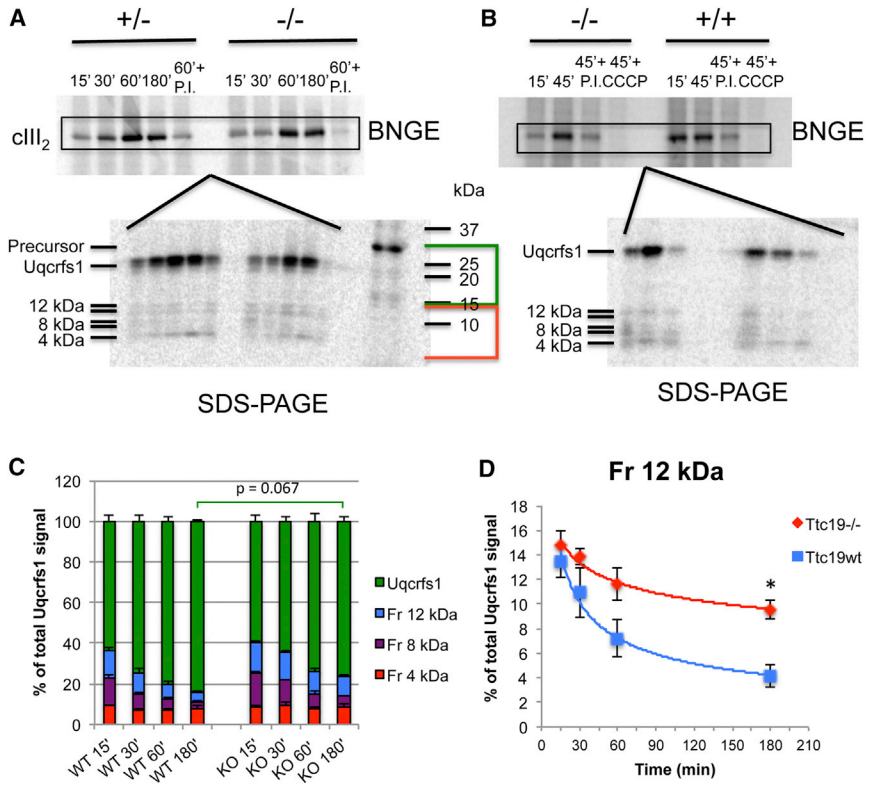

Figure 4. UQCRFS1-Derived Fragments Are Cleared More Rapidly in the Presence of TTC19

(A) Isolated mitochondria from *Ttc19*$^{-/-}$ and *Ttc19*^{WT} (*Ttc19*$^{+/-}$) mouse liver were incubated with ^{35}S-labeled UQCRFS1 at different times (15, 30, and 60 min). After a 60-min incubation, mitochondria were washed and the incubation continued for another 2 hr (chase; 180 min total incubation time). A fraction of the mitochondria was also incubated for 60 min in the presence of a protease inhibitor cocktail (P.I.). After the 1D-BNGE, the band corresponding to cIII$_2$ was cut, denatured, and run through SDS-PAGE, together with the *in vitro* labeled UQCRFS1 (precursor). The radioactive signals were visualized by phosphor-imaging.

(B) Isolated mitochondria from *Ttc19*$^{-/-}$ and *Ttc19*$^{+/+}$ (*Ttc19*^{WT}) mouse liver were incubated with ^{35}S-labeled UQCRFS1 at 15 and 45 min in the absence or presence of protease inhibitor cocktail (P.I.). After the 1D-BNGE, the band corresponding to cIII$_2$ was cut, denatured, and run through SDS-PAGE, together with the *in vitro* labeled UQCRFS1 (precursor). The radioactive signals were visualized by phosphor-imaging.

(C) The relative proportion of the UQCRFS1 fragments versus the mature protein in the SDS-PAGE was quantified by densitometry (ImageJ). The percentage of the total UQCRFS1 signal for each of the species, classified according to their calculated molecular mass, in the *Ttc19*$^{-/-}$ and *Ttc19*^{WT} samples during the time course shown in (A) was plotted. Values are mean ± SEM of three independent experiments. Statistical analysis was by unpaired Student's t test.

(D) The percentage of 12-kDa fragments remaining in each time point (15, 30, 60, and 180 min) for *Ttc19*$^{-/-}$ and *Ttc19*^{WT} were adjusted to an exponential one-phase decay curve. Error bars represent SEM (n = 3); statistical analysis was by unpaired Student's t test (*p < 0.05).

(E) UQCRFS1 amino acid sequence coverage of the peptides detected by mass spectrometry. The analysis was performed in three biological replicates for each genotype, separating the upper part of the SDS-PAGE gel (area covering from 30 to 14 kDa; in green) and the lower part of the gel (from 14 kDa to the Coomassie blue front; in red).

See also Figure S6.

both 12- and 8-kDa fragments was slower in the *Ttc19*$^{-/-}$ versus *Ttc19*^{WT} samples (Figure 4C), and this difference was significant for the 12-kDa fragment at 180 min (p = 0.02) (Figure 4D). The reduced clearance of UQCRFS1 fragments over time can explain their accumulation in steady-state conditions (Figure 3D), and it suggests a specific role for TTC19 as a husbandry factor in the turnover of damaged UQCRFS1 within cIII$_2$. Finally, we observed reduced incorporation of UQCRFS1 in the presence of a general protease inhibitor cocktail, indicating that proteolytic processing is necessary for the correct insertion of this subunit into cIII$_2$. The action of proteases is also necessary for the clearance of the UQCRFS1 fragments, because their relative amounts versus mature UQCRFS1 remained the same as in the 15-min pulse (Figure 4B).

Identification of the UQCRFS1-Derived Fragments

To gain insight into the identity of the accumulated fragments derived from UQCRFS1, we again electrophoresed the cIII$_2$ band from three *Ttc19*^{WT} and three *Ttc19*$^{-/-}$ samples from liver mitochondria. Each of the gel lanes were cut into slices and analyzed by mass spectrometry after tryptic digestion. The gel was divided into two sections, one encompassing the protein species from 30 to 14 kDa, where the mature UQCRFS1 is found (calculated molecular weight [MW]: 21.5 kDa), whereas the second one encompassed the interval from 14 kDa to the Coomassie blue dye front of the gel, where the UQCRFS1 fragments were detected. In the 30- to 14-kDa section, we consistently detected tryptic peptides covering the full length of processed, mature UQCRFS1, without the 78 N-terminal amino acid-long MTS

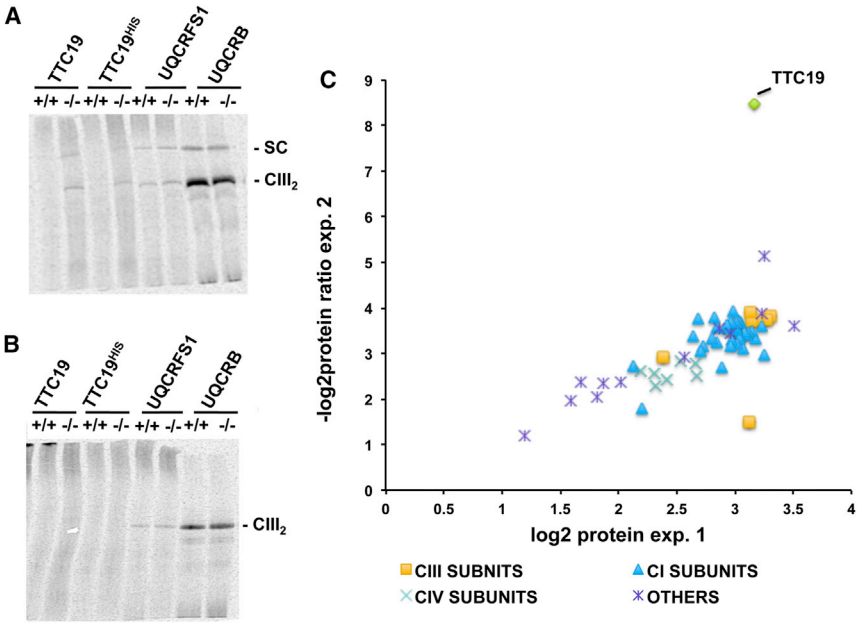

Figure 5. TTC19 Interacts with $cIII_2$ and SC

(A and B) *In organello* import of ^{35}S-labeled hTTC19, hTTC19^{6HIS}, Uqcrfs1, and Uqcrb. *Ttc19*^{WT} and *Ttc19*$^{-/-}$ mitochondria were solubilized in (A) digitonin or (B) DDM and run on 1D-BNGE. Uqcrfs1 and Uqcrb were used for $cIII_2$ visualization.

(C) Scatterplot showing proteins interacting with hTTC19^{FLAG}. The data were obtained by mass spectrometry analysis of fractions from HEK293T cells grown in SILAC media and immunoprecipitated with anti-FLAG-conjugated agarose beads. Each cell line was labeled with both heavy and light amino acids. Before mitoplast generation and solubilization, differentially labeled HEK cells expressing hTTC19^{FLAG} were combined with naive cells in a 1:1 ratio. The values on the x axis come from experiment 1, i.e., heavy-labeled hTTC19^{FLAG} HEK293T cells mixed with the light-labeled naive cells, and the y axis represents the values of experiment 2, i.e., light-labeled hTTC19^{FLAG} HEK293T cells mixed with the heavy-labeled naive cells. Only the proteins showing a statistically significant log_2 enrichment ratio in both experiments are plotted.

See also Figure S7 and Table S1.

(Brandt et al., 1993). Conversely, in the 14 kDa-dye front section of the gel, peptides corresponding to the MTS/Su9 were consistently detected in both *Ttc19*^{WT} and *Ttc19*$^{-/-}$ samples, along with other peptides corresponding to the rest of the UQCRFS1 sequence, with the exception of the C-terminal end (Figure 4D).

Physical Interaction of TTC19 with $cIII_2$

To further characterize the proposed direct interaction of TTC19 with $cIII_2$ (Ghezzi et al., 2011), we performed *in organello* import experiments using *in vitro* translated ^{35}S-labeled hTTC19 followed by BNGE. In digitonin-treated samples, we detected ^{35}S-hTTC19 in bands corresponding to the $cIII_2$ holocomplex and $cIII_2$-containing supercomplexes (SCs). Newly incorporated ^{35}S-hTTC19 was detected only in *Ttc19*$^{-/-}$, but not in *Ttc19*^{WT}, mitochondria, suggesting that the interaction of the endogenous Ttc19 with $cIII_2$ prevents its dislodgment by ^{35}S-hTTC19. However, this interaction must be relatively labile, since no ^{35}S-hTTC19 signal was detected in mitochondria treated with DDM, a detergent stronger than digitonin (Figures 5A and 5B).

To test whether the TTC19 migration in BNGE is due to its physical interaction with $cIII_2$, we then performed co-immunoprecipitation assays using a HEK293T cell line expressing a FLAG-tagged recombinant human TTC19 (*hTTC19*^{FLAG}). We first showed that hTTC19^{FLAG} was robustly expressed in these cells upon doxycycline induction (Figure S7A) and was co-immunoprecipitated with UQCRFS1 and UQCRC2 (Figure S7B).

The protein interactions of hTTC19^{FLAG} were further analyzed by quantitative mass spectrometry analysis of mitoplasts from naive and recombinant HEK293T cells after FLAG immunopurification. Comparisons were enabled by stable isotopic labeling of amino acids in cell culture (SILAC). From duplicate, reciprocal-labeling experiments (see the STAR Methods for details), a total of 64 proteins was quantitatively different in the hTTC19^{FLAG} versus naive samples (Figure 5C; Table S1). Of these 64 proteins, 51 were components of the respiratory chain, including eight subunits of $cIII_2$, as well as numerous subunits of cI and cIV (Table S1). These data demonstrate that hTTC19^{FLAG} co-purifies with $cIII_2$ holocomplex, as well as with $cIII_2$-containing SCs. Interestingly, the mitochondrial proteases YME1L and PARL, together with the scaffold protein STOML2 (SLP2), all three members of the SPY complex (Wai et al., 2016), were also co-immunopurified with TTC19, indicating physical interaction (Table S1).

Kinetics of TTC19 Incorporation into $cIII_2$

To explore the role of TTC19 in $cIII_2$ biogenesis, we analyzed three different $cIII_2$-deficient cell lines: a *TTC19*-less human fibroblast cell line (Ghezzi et al., 2011), two *BCS1L*-mutated human fibroblast cell lines (Fernandez-Vizarra et al., 2007), and a recombinant HeLa cell line overexpressing MZM1L/LYRM7^{HA} (Sánchez et al., 2013). The latter two cell lines showed a strong reduction in the levels of UQCRFS1 present in $cIII_2$ (Figure 6A), since BCS1L is a late-stage assembly factor necessary for UQCRFS1 incorporation (Fernandez-Vizarra et al., 2007), whereas overexpression of LYRM7, which physically interacts with UQCRFS1, causes UQCRFS1 to be sequestered in the mitochondrial matrix, thus preventing its incorporation into $cIII_2$ (Sánchez et al., 2013).

Immunodetection of 1D-BNGE (Figure 6A) and 2D-BNGE (Figure 6B) revealed that the lack of TTC19 did not prevent UQCRFS1 from being incorporated into $cIII_2$ and SC, since comparable levels were found in control and TTC19-less fibroblasts. In addition, a substantial amount of TTC19 co-migrated with $cIII_2$, $cIII_2$ + cIV, and SC in control cell lines (Figure 6B), confirming the data from quantitative mass spectrometry and *in organello* import. Conversely, in both *BCS1L* mutant and LYRM7^{HA}-overexpressing cells, TTC19 (Figure 6C) and residual UQCRFS1

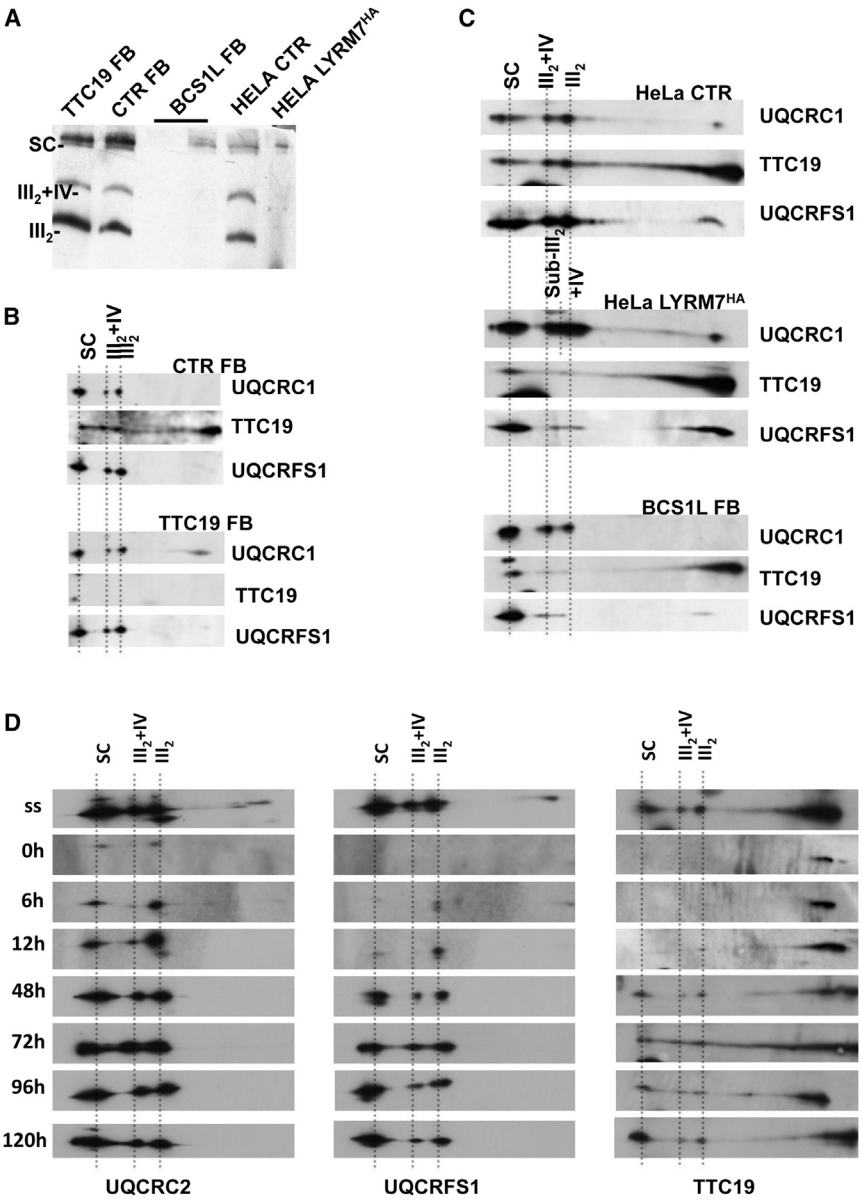

Figure 6. TTC19 Interacts with cIII$_2$ via UQCRFS1

(A) 1D-BNGE and western blot analysis of digitonin-treated immortalized skin fibroblasts from control (CTR FB), TTC19-less (TTC19 FB), and BCS1L mutant (BCS1L FB) cell lines, as well as HeLa cells overexpressing LYRM7^{HA} and its corresponding empty vector control (HELA CTR). The blot was immunodetected using an anti-UQCRFS1 antibody.

(B) A sample of BCS1L FB was run on a 2D-BNGE and immunodetected with the indicated antibodies.

(C) A sample of HeLa cells overexpressing LYRM7^{HA} was run on a 2D-BNGE and immunodetected with the indicated antibodies.

(D) HEK293T cells were treated for 8 days with 15 μg/mL doxycycline and collected (t = 0 hr). Doxycycline was then removed to let the mitochondrial respiratory chain assembly recover, and cells were collected at the indicated times. Samples were run on a 2D-BNGE and immunodetected with the indicated antibodies. Steady-state (ss) level was used for comparison.

were both present in SC, but they were virtually absent in free cIII$_2$ and cIII$_2$ + cIV spots (Figures 6A and 6C).

Next, the kinetics of cIII$_2$ assembly in control HEK293T cells was investigated by treating them for 8 days with 15 μg/mL doxycycline, a reversible inhibitor of mitochondrial translation (Moreno-Lastres et al., 2012; Ugalde et al., 2004). After removal of the drug, the incorporation of UQCRFS1, UQCRC2, and TTC19 into cIII$_2$ was followed over time by immunodetection of 2D-BNGE of digitonin-treated mitochondria. As shown in Figure 6D, UQCRFS1 was incorporated later than UQCRC2 in cIII$_2$-containing SC, cIII$_2$-cIV, and cIII$_2$ holocomplex, whereas TTC19 showed the same kinetics of UQCRFS1.

Altogether these results indicate that TTC19 interacts with the mature form of cIII$_2$ (i.e., after UQCRFS1 incorporation) and is not necessary for the incorporation of UQCRFS1 itself.

DISCUSSION

Loss-of-function mutations in *TTC19* have been found in patients with cIII$_2$ deficiency associated with heterogeneous neurological syndromes (Ardissone et al., 2015; Atwal, 2014; Ghezzi et al., 2011; Kunii et al., 2015; Melchionda et al., 2014; Mordaunt et al., 2015; Morino et al., 2014; Nogueira et al., 2013). *TTC19* ablation in *D. melanogaster* causes cIII$_2$ deficiency associated with a neurological phenotype in adult flies (Ghezzi et al., 2011). Likewise, our *Ttc19*$^{-/-}$ mice showed slowly progressive impairment of neurological skills; reduced energy metabolism; and low cIII$_2$ activity in brain, liver, and skeletal muscle. These results clearly indicate that TTC19 plays a role in maintaining cIII$_2$ integrity and function in multicellular animals, thus preventing progressive neurological impairment. As a consequence of cIII$_2$ deficiency, especially when UQCRFS1 fails to be incorporated, ROS production increases (Brand, 2010; Diaz et al., 2012; Hinson et al., 2007; Morán et al., 2010). This elevated oxidative stress, which we have confirmed to occur in our *Ttc19*$^{-/-}$ mouse, is likely to contribute to the pathology of the disease associated to *TTC19* mutations.

The availability of a constitutive *Ttc19*$^{-/-}$ mouse and of a set of human cellular models allowed us to gain insight into the mechanism of action of TTC19. First, we demonstrated that *Ttc19*$^{-/-}$-associated cIII$_2$ holocomplex displays an aberrant electrophoretic behavior in Coomassie-stained BNGE. The altered mobility and reduced focalization of cIII$_2$-specific 1D-BNGE bands were confirmed by complexome profiling of *Ttc19*$^{-/-}$ mitochondria. However, the subunit composition of cIII$_2$ did not differ between

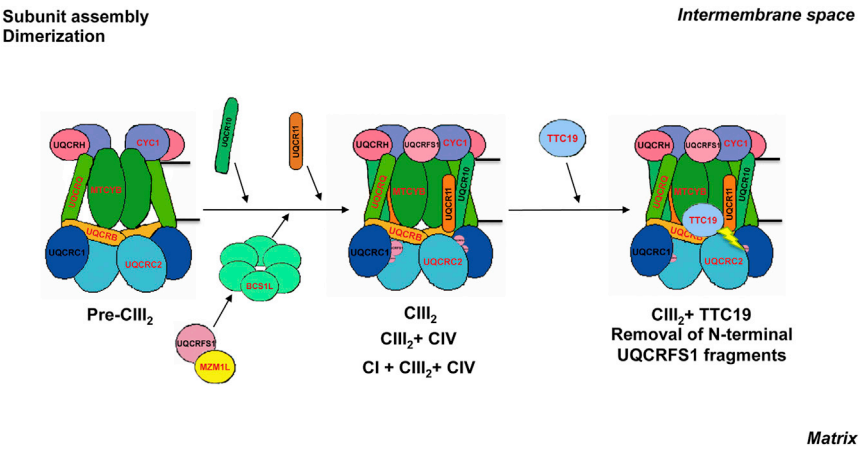

Figure 7. Late Steps of $cIII_2$ Assembly in Mammalian Mitochondria

Model depicting the last phase in $cIII_2$ assembly where UQCRFS1 is incorporated and processed *in situ*. TTC19 is then bound to mature $cIII_2$ to perform its husbandry role in eliminating the N-terminal fragments generated during UQCRFS1 assembly.

Ttc19^{WT} and *Ttc19*$^{-/-}$ mitochondria, suggesting a subtler change to the $cIII_2$ structure rather than drastically impaired $cIII_2$ assembly. Second, in solid tissues of *Ttc19*$^{-/-}$ mice, we detected reduced amounts of intact mature UQCRFS1 with the accumulation of UQCRFS1-derived fragments. Our import kinetic experiments show that UQCRFS1 processing occurs rapidly after its assembly. The maturation of UQCRFS1 by processing its precursor, through the cleavage of the N-terminal 78 amino acids, was found to occur *in situ,* once the protein is incorporated into $cIII_2$ (Brandt et al., 1993; Graham et al., 1994). The MTS polypeptide was proposed to remain as a structural component of mammalian $cIII_2$ and was identified as Su9 (Borchart et al., 1985; Brandt et al., 1993; Schägger et al., 1985). In the bovine $cIII_2$ X-ray diffraction structures, Su9 is found between UQCRC1 and UQCRC2 (Iwata et al., 1998), which are homologous to the two subunits of the matrix-processing peptidase (MPP). They also possess protease activity that is inhibited by the binding of UQCRFS1 N-terminal peptides (Deng et al., 1998, 2001). According to the crystal structure, the proteolytic site lies exactly between the N terminus of the mature UQCRFS1 and Su9. However, only a stretch of 33 amino acids of Su9 is resolved in the 3-Å structure (Iwata et al., 1998).

We show here that several species (12, 8, and 4 kDa) are generated in UQCRFS1 maturation, most probably due to the endogenous $cIII_2$ MPP activity. We think that the $cIII_2$-bound 8-kDa fragment was purified in the experiments that led to the original identification of Su9 (Borchart et al., 1985; Brandt et al., 1993; Schägger et al., 1985); this peptide corresponds exactly to the 78 N-terminal amino acids of UQCRFS1. However, the identification of this fragment does not necessarily imply that it must be considered a structural subunit of $cIII_2$, as we showed that additional fragments from UQCRFS1 are also present in the context of holo-$cIII_2$. In fact, the results presented here clearly show that there is a specific clearance of the 12- and 8-kDa fragments, which is impaired in the absence of TTC19. In turn, impaired clearance is likely to determine conformational and structural heterogeneity of mature $cIII_2$, thus accounting for the aberrant electrophoretic mobility of the complex shown in 1D-BNGE. This in turn is associated with impaired $cIII_2$ catalytic activity and increased ROS production. One possibility is that the persistence of UQCRFS1-derived fragments may prevent newly imported UQCRFS1 precursor to be processed/assembled into $cIII_2$, as suggested by the lower amounts of mature UQCRFS1 incorporated in $cIII_2$ from *Ttc19*$^{-/-}$ tissues. These findings, together with the kinetic and steady-state data, show that in physiological conditions the small UQCRFS1-derived fragments are cleared from the $cIII_2$ holocomplex, which indicates a role for the N-terminal part of UQCRFS1 in the regulation of $cIII_2$ function as well as a related quality control function for TTC19.

Our *in organello* import, quantitative mass spectrometry analysis, and co-immunoprecipitation assays clearly demonstrate that TTC19 physically interacts with $cIII_2$ and with $cIII_2$-containing SCs ($cIII_2$ + cIV and cI + $cIII_2$ + cIV). In addition, using a set of suitable human cell models, in which UQCRFS1 incorporation is impaired, as well as kinetic experiments, we have shown that TTC19 is incorporated into $cIII_2$ species only after its assembly is completed, i.e., after the incorporation of the last catalytic subunit, UQCRFS1. The assembly of $cIII_2$ proceeds normally in the absence of TTC19, as shown in the patient-derived fibroblasts and in *Ttc19*$^{-/-}$ mouse mitochondria. This is compatible with a role for TTC19 in removing the N-terminal products of UQCRFS1 processing *in situ,* once it is assembled.

Our results demonstrate that mitochondria of pluricellular animals have developed a system in which TTC19 acts as a husbandry factor involved in the clearance of the UQCRFS1 fragments, whose presence within the $cIII_2$ structure is detrimental for its catalytic activity. TTC19 could be acting in collaboration with mitochondrial proteases to get rid of the UQCRFS1-processed peptides (see the model proposed in Figure 7). In line with this idea, we found an interaction of TTC19 with the components of the recently discovered large inner membrane protease complex SLP2-PARL-YME1L (SPY) (Wai et al., 2016). Whether all these factors collaborate together in a specific $cIII_2$ quality control pathway is a matter of great interest that will be further investigated.

In conclusion, we propose that the main role of TTC19 is to preserve the structural and functional integrity of $cIII_2$ and the lack of this post-assembly quality control role causes $cIII_2$ deficiency, increased ROS production, and organ failure.

STAR★METHODS

Detailed methods are provided in the online version of this paper and include the following:

- KEY RESOURCES TABLE
- CONTACT FOR REAGENT AND RESOURCE SHARING

- METHOD DETAILS
  - Cell Culture and Transfection
  - BNGE
  - Western Blot
  - *In Organello* Import of Radiolabeled Proteins
  - Generation of Ttc19$^{-/-}$ Mice
  - Behavioral and Locomotor Analysis
  - Construction of AAV2/8 Vector
  - Biochemical Analysis of MRC Complexes
  - Morphological Analysis
  - ROS Measurement
  - Proteomics
  - Statistical Analysis

SUPPLEMENTAL INFORMATION

Supplemental Information includes seven figures and one table and can be found with this article online at http://dx.doi.org/10.1016/j.molcel.2017.06.001.

AUTHOR CONTRIBUTIONS

E.B., C.V., E.F.-V., and M.Z. conceived the project, designed the experimental outline, and wrote the manuscript. E.B. characterized the Ttc19$^{-/-}$ mouse model, with the help of C.V., and performed the molecular biology and biochemistry work in mouse tissues and cell lines, with the help of S.A.D. E.F.-V. performed the *in organello* import and incorporation experiments. R.C., C.G., and G.D. characterized the brain and skeletal muscle histopathology. M.E.H. and I.M.F. were responsible for mass spectrometry and complexome analyses. S.R. performed the statistical analyses.

ACKNOWLEDGMENTS

We would like to thank Dr. Daniele Ghezzi for critically reading the manuscript and Sujing Ding of the MRC-MBU Mass Spectrometry Facility for excellent assistance to this work. We are grateful to the personnel at Phenomics and ARES animal care facilities for skillful technical assistance. We thank Professor Alberto Auricchio and the TIGEM vector core facility for the production of the AAV2/8 viral stock. This work was supported by the Core Grant from the MRC, ERC advanced grant FP7-322424 and NRJ-Institut de France Grant (to M.Z.), and Association Française contre les Myopathies (AFM) grant 16086 (to E.F.-V.).

Received: February 27, 2017
Revised: April 3, 2017
Accepted: June 1, 2017
Published: June 29, 2017

REFERENCES

Andrews, B., Carroll, J., Ding, S., Fearnley, I.M., and Walker, J.E. (2013). Assembly factors for the membrane arm of human complex I. Proc. Natl. Acad. Sci. USA *110*, 18934–18939.

Ardissone, A., Granata, T., Legati, A., Diodato, D., Melchionda, L., Lamantea, E., Garavaglia, B., Ghezzi, D., and Moroni, I. (2015). Mitochondrial complex III deficiency caused by TTC19 defects: report of a novel mutation and review of literature. JIMD Rep. *22*, 115–120.

Atwal, P.S. (2014). Mutations in the complex III assembly factor tetratricopeptide 19 gene TTC19 are a rare cause of Leigh syndrome. JIMD Rep. *14*, 43–45.

Borchart, U., Machleidt, W., Schägger, H., Link, T.A., and von Jagow, G. (1985). Isolation and amino acid sequence of the 8 kDa DCCD-binding protein of beef heart ubiquinol:cytochrome c reductase. FEBS Lett. *191*, 125–130.

Borek, A., Sarewicz, M., and Osyczka, A. (2008). Movement of the iron-sulfur head domain of cytochrome bc(1) transiently opens the catalytic Q(o) site for reaction with oxygen. Biochemistry *47*, 12365–12370.

Brand, M.D. (2010). The sites and topology of mitochondrial superoxide production. Exp. Gerontol. *45*, 466–472.

Brandt, U., Yu, L., Yu, C.A., and Trumpower, B.L. (1993). The mitochondrial targeting presequence of the Rieske iron-sulfur protein is processed in a single step after insertion into the cytochrome bc1 complex in mammals and retained as a subunit in the complex. J. Biol. Chem. *268*, 8387–8390.

Brunetti, D., Torsvik, J., Dallabona, C., Teixeira, P., Sztromwasser, P., Fernandez-Vizarra, E., Cerutti, R., Reyes, A., Preziuso, C., D'Amati, G., et al. (2016). Defective PITRM1 mitochondrial peptidase is associated with Aβ amyloidotic neurodegeneration. EMBO Mol. Med. *8*, 176–190.

Cox, J., and Mann, M. (2008). MaxQuant enables high peptide identification rates, individualized p.p.b.-range mass accuracies and proteome-wide protein quantification. Nat. Biotechnol. *26*, 1367–1372.

Dallabona, C., Abbink, T.E., Carrozzo, R., Torraco, A., Legati, A., van Berkel, C.G., Niceta, M., Langella, T., Verrigni, D., Rizza, T., et al. (2016). LYRM7 mutations cause a multifocal cavitating leukoencephalopathy with distinct MRI appearance. Brain *139*, 782–794.

de Lonlay, P., Valnot, I., Barrientos, A., Gorbatyuk, M., Tzagoloff, A., Taanman, J.W., Benayoun, E., Chrétien, D., Kadhom, N., Lombès, A., et al. (2001). A mutant mitochondrial respiratory chain assembly protein causes complex III deficiency in patients with tubulopathy, encephalopathy, and liver failure. Nat. Genet. *29*, 57–60.

Deng, K., Zhang, L., Kachurin, A.M., Yu, L., Xia, D., Kim, H., Deisenhofer, J., and Yu, C.A. (1998). Activation of a matrix processing peptidase from the crystalline cytochrome bc1 complex of bovine heart mitochondria. J. Biol. Chem. *273*, 20752–20757.

Deng, K., Shenoy, S.K., Tso, S.C., Yu, L., and Yu, C.A. (2001). Reconstitution of mitochondrial processing peptidase from the core proteins (subunits I and II) of bovine heart mitochondrial cytochrome bc(1) complex. J. Biol. Chem. *276*, 6499–6505.

Diaz, F., Enríquez, J.A., and Moraes, C.T. (2012). Cells lacking Rieske iron-sulfur protein have a reactive oxygen species-associated decrease in respiratory complexes I and IV. Mol. Cell. Biol. *32*, 415–429.

Dröse, S., and Brandt, U. (2008). The mechanism of mitochondrial superoxide production by the cytochrome bc1 complex. J. Biol. Chem. *283*, 21649–21654.

Fellman, V. (2002). The GRACILE syndrome, a neonatal lethal metabolic disorder with iron overload. Blood Cells Mol. Dis. *29*, 444–450.

Fernández-Vizarra, E., and Zeviani, M. (2015). Nuclear gene mutations as the cause of mitochondrial complex III deficiency. Front. Genet. *6*, 134.

Fernandez-Vizarra, E., Bugiani, M., Goffrini, P., Carrara, F., Farina, L., Procopio, E., Donati, A., Uziel, G., Ferrero, I., and Zeviani, M. (2007). Impaired complex III assembly associated with BCS1L gene mutations in isolated mitochondrial encephalopathy. Hum. Mol. Genet. *16*, 1241–1252.

Fernández-Vizarra, E., Ferrín, G., Pérez-Martos, A., Fernández-Silva, P., Zeviani, M., and Enríquez, J.A. (2010). Isolation of mitochondria for biogenetical studies: an update. Mitochondrion *10*, 253–262.

Gao, G., Qu, G., Burnham, M.S., Huang, J., Chirmule, N., Joshi, B., Yu, Q.C., Marsh, J.A., Conceicao, C.M., and Wilson, J.M. (2000). Purification of recombinant adeno-associated virus vectors by column chromatography and its performance in vivo. Hum. Gene Ther. *11*, 2079–2091.

Ghezzi, D., Arzuffi, P., Zordan, M., Da Re, C., Lamperti, C., Benna, C., D'Adamo, P., Diodato, D., Costa, R., Mariotti, C., et al. (2011). Mutations in TTC19 cause mitochondrial complex III deficiency and neurological impairment in humans and flies. Nat. Genet. *43*, 259–263.

Graham, L.A., Brandt, U., and Trumpower, B.L. (1994). Protease maturation of the Rieske iron-sulphur protein after its insertion into the mitochondrial cytochrome bc1 complex of Saccharomyces cerevisiae. Biochem. Soc. Trans. *22*, 188–191.

Gruschke, S., Römpler, K., Hildenbeutel, M., Kehrein, K., Kühl, I., Bonnefoy, N., and Ott, M. (2012). The Cbp3-Cbp6 complex coordinates cytochrome b

synthesis with bc(1) complex assembly in yeast mitochondria. J. Cell Biol. *199*, 137–150.

Heide, H., Bleier, L., Steger, M., Ackermann, J., Dröse, S., Schwamb, B., Zörnig, M., Reichert, A.S., Koch, I., Wittig, I., and Brandt, U. (2012). Complexome profiling identifies TMEM126B as a component of the mitochondrial complex I assembly complex. Cell Metab. *16*, 538–549.

Hildenbeutel, M., Hegg, E.L., Stephan, K., Gruschke, S., Meunier, B., and Ott, M. (2014). Assembly factors monitor sequential hemylation of cytochrome b to regulate mitochondrial translation. J. Cell Biol. *205*, 511–524.

Hinson, J.T., Fantin, V.R., Schönberger, J., Breivik, N., Siem, G., McDonough, B., Sharma, P., Keogh, I., Godinho, R., Santos, F., et al. (2007). Missense mutations in the BCS1L gene as a cause of the Björnstad syndrome. N. Engl. J. Med. *356*, 809–819.

Invernizzi, F., Tigano, M., Dallabona, C., Donnini, C., Ferrero, I., Cremonte, M., Ghezzi, D., Lamperti, C., and Zeviani, M. (2013). A homozygous mutation in LYRM7/MZM1L associated with early onset encephalopathy, lactic acidosis, and severe reduction of mitochondrial complex III activity. Hum. Mutat. *34*, 1619–1622.

Iwata, S., Lee, J.W., Okada, K., Lee, J.K., Iwata, M., Rasmussen, B., Link, T.A., Ramaswamy, S., and Jap, B.K. (1998). Complete structure of the 11-subunit bovine mitochondrial cytochrome bc1 complex. Science *281*, 64–71.

Kirby, D.M., Thorburn, D.R., Turnbull, D.M., and Taylor, R.W. (2007). Biochemical assays of respiratory chain complex activity. Methods Cell Biol. *80*, 93–119.

Kunii, M., Doi, H., Higashiyama, Y., Kugimoto, C., Ueda, N., Hirata, J., Tomita-Katsumoto, A., Kashikura-Kojima, M., Kubota, S., Taniguchi, M., et al. (2015). A Japanese case of cerebellar ataxia, spastic paraparesis, and deep sensory impairment associated with a novel homozygous TTC19 mutation. J. Hum. Genet. *60*, 187–191.

Manczak, M., Anekonda, T.S., Henson, E., Park, B.S., Quinn, J., and Reddy, P.H. (2006). Mitochondria are a direct site of A beta accumulation in Alzheimer's disease neurons: implications for free radical generation and oxidative damage in disease progression. Hum. Mol. Genet. *15*, 1437–1449.

Melchionda, L., Damseh, N.S., Abu Libdeh, B.Y., Nasca, A., Elpeleg, O., Zanolini, A., and Ghezzi, D. (2014). A novel mutation in TTC19 associated with isolated complex III deficiency, cerebellar hypoplasia, and bilateral basal ganglia lesions. Front. Genet. *5*, 397.

Morán, M., Marín-Buera, L., Gil-Borlado, M.C., Rivera, H., Blázquez, A., Seneca, S., Vázquez-López, M., Arenas, J., Martín, M.A., and Ugalde, C. (2010). Cellular pathophysiological consequences of BCS1L mutations in mitochondrial complex III enzyme deficiency. Hum. Mutat. *31*, 930–941.

Mordaunt, D.A., Jolley, A., Balasubramaniam, S., Thorburn, D.R., Mountford, H.S., Compton, A.G., Nicholl, J., Manton, N., Clark, D., Bratkovic, D., et al. (2015). Phenotypic variation of TTC19-deficient mitochondrial complex III deficiency: a case report and literature review. Am. J. Med. Genet. A. *167*, 1330–1336.

Moreno-Lastres, D., Fontanesi, F., García-Consuegra, I., Martín, M.A., Arenas, J., Barrientos, A., and Ugalde, C. (2012). Mitochondrial complex I plays an essential role in human respirasome assembly. Cell Metab. *15*, 324–335.

Morino, H., Miyamoto, R., Ohnishi, S., Maruyama, H., and Kawakami, H. (2014). Exome sequencing reveals a novel TTC19 mutation in an autosomal recessive spinocerebellar ataxia patient. BMC Neurol. *14*, 5.

Nijtmans, L.G., Henderson, N.S., and Holt, I.J. (2002). Blue Native electrophoresis to study mitochondrial and other protein complexes. Methods *26*, 327–334.

Nogueira, C., Barros, J., Sá, M.J., Azevedo, L., Taipa, R., Torraco, A., Meschini, M.C., Verrigni, D., Nesti, C., Rizza, T., et al. (2013). Novel TTC19 mutation in a family with severe psychiatric manifestations and complex III deficiency. Neurogenetics *14*, 153–160.

Ramos-Arroyo, M.A., Hualde, J., Ayechu, A., De Meirleir, L., Seneca, S., Nadal, N., and Briones, P. (2009). Clinical and biochemical spectrum of mitochondrial complex III deficiency caused by mutations in the BCS1L gene. Clin. Genet. *75*, 585–587.

Salmon, P., Oberholzer, J., Occhiodoro, T., Morel, P., Lou, J., and Trono, D. (2000). Reversible immortalization of human primary cells by lentivector-mediated transfer of specific genes. Mol. Ther. *2*, 404–414.

Sánchez, E., Lobo, T., Fox, J.L., Zeviani, M., Winge, D.R., and Fernández-Vizarra, E. (2013). LYRM7/MZM1L is a UQCRFS1 chaperone involved in the last steps of mitochondrial complex III assembly in human cells. Biochim. Biophys. Acta *1827*, 285–293.

Schägger, H., Borchart, U., Aquila, H., Link, T.A., and von Jagow, G. (1985). Isolation and amino acid sequence of the smallest subunit of beef heart bc1 complex. FEBS Lett. *190*, 89–94.

Schindelin, J., Arganda-Carreras, I., Frise, E., Kaynig, V., Longair, M., Pietzsch, T., Preibisch, S., Rueden, C., Saalfeld, S., Schmid, B., et al. (2012). Fiji: an open-source platform for biological-image analysis. Nat. Methods *9*, 676–682.

Sciacco, M., and Bonilla, E. (1996). Cytochemistry and immunocytochemistry of mitochondria in tissue sections. Methods Enzymol. *264*, 509–521.

Skarnes, W.C., Rosen, B., West, A.P., Koutsourakis, M., Bushell, W., Iyer, V., Mujica, A.O., Thomas, M., Harrow, J., Cox, T., et al. (2011). A conditional knockout resource for the genome-wide study of mouse gene function. Nature *474*, 337–342.

Smith, P.M., Fox, J.L., and Winge, D.R. (2012). Biogenesis of the cytochrome bc(1) complex and role of assembly factors. Biochim. Biophys. Acta *1817*, 276–286.

Song, M., Chen, Y., Gong, G., Murphy, E., Rabinovitch, P.S., and Dorn, G.W., 2nd (2014). Super-suppression of mitochondrial reactive oxygen species signaling impairs compensatory autophagy in primary mitophagic cardiomyopathy. Circ. Res. *115*, 348–353.

Tucker, E.J., Wanschers, B.F., Szklarczyk, R., Mountford, H.S., Wijeyeratne, X.W., van den Brand, M.A., Leenders, A.M., Rodenburg, R.J., Reljić, B., Compton, A.G., et al. (2013). Mutations in the UQCC1-interacting protein, UQCC2, cause human complex III deficiency associated with perturbed cytochrome b protein expression. PLoS Genet. *9*, e1004034.

Tyanova, S., Temu, T., Sinitcyn, P., Carlson, A., Hein, M.Y., Geiger, T., Mann, M., and Cox, J. (2016). The Perseus computational platform for comprehensive analysis of (prote)omics data. Nat. Methods *13*, 731–740.

Ugalde, C., Vogel, R., Huijbens, R., Van Den Heuvel, B., Smeitink, J., and Nijtmans, L. (2004). Human mitochondrial complex I assembles through the combination of evolutionary conserved modules: a framework to interpret complex I deficiencies. Hum. Mol. Genet. *13*, 2461–2472.

Wai, T., Saita, S., Nolte, H., Müller, S., König, T., Richter-Dennerlein, R., Sprenger, H.G., Madrenas, J., Mühlmeister, M., Brandt, U., et al. (2016). The membrane scaffold SLP2 anchors a proteolytic hub in mitochondria containing PARL and the i-AAA protease YME1L. EMBO Rep. *17*, 1844–1856.

Wanschers, B.F., Szklarczyk, R., van den Brand, M.A., Jonckheere, A., Suijskens, J., Smeets, R., Rodenburg, R.J., Stephan, K., Helland, I.B., Elkamil, A., et al. (2014). A mutation in the human CBP4 ortholog UQCC3 impairs complex III assembly, activity, and cytochrome b stability. Hum. Mol. Genet. *23*, 6356–6365.

Wittig, I., Braun, H.P., and Schägger, H. (2006). Blue native PAGE. Nat. Protoc. *1*, 418–428.

Wittig, I., Karas, M., and Schägger, H. (2007). High resolution clear native electrophoresis for in-gel functional assays and fluorescence studies of membrane protein complexes. Mol. Cell. Proteomics *6*, 1215–1225.

Xiao, W., Chirmule, N., Berta, S.C., McCullough, B., Gao, G., and Wilson, J.M. (1999). Gene therapy vectors based on adeno-associated virus type 1. J. Virol. *73*, 3994–4003.

Zara, V., Conte, L., and Trumpower, B.L. (2009). Biogenesis of the yeast cytochrome bc1 complex. Biochim. Biophys. Acta *1793*, 89–96.

STAR★METHODS

KEY RESOURCES TABLE

REAGENT or RESOURCE	SOURCE	IDENTIFIER
Antibodies		
Mouse monoclonal anti-UQCRC1	Abcam	Cat#ab110252; RRID: AB_10863633
Mouse monoclonal anti-UQCRC2	Abcam	Cat#ab14745; RRID: AB_2213640
Mouse monoclonal anti-UQCRFS1	Abcam	Cat#ab14746; RRID: AB_301445
Mouse monoclonal anti-UQCRQ	Abcam	Cat#ab110255; RRID: AB_10865309
Rabbit polyclonal anti-CYC1	Sigma	Cat#HPA001247; RRID: AB_1078602
Rabbit polyclonal anti-UQCRB	Proteintech	Cat#10756-1-AP; RRID: AB_2304256
Rabbit polyclonal anti-CD68	Abcam	Cat#ab125212; RRID: AB_10975465
Rabbit polyclonal anti-Ubiquitin	Abcam	Cat#ab7780; RRID: AB_306069
Rabbit polyclonal anti-Amyloid Precursor Protein	Abcam	Cat#ab15272; RRID: AB_301808
Mouse monoclonal anti-200 kD Neurofilament Heavy	Abcam	Cat#ab7795; RRID: AB_306084
Rabbit polyclonal anti-Tau (phospho T212)	Abcam	Cat#ab51053; RRID: AB_882853
Mouse monoclonal anti-Neuronal Nuclei (NeuN)	Millipore	Cat#MAB377; RRID: AB_2298772
Rabbit polyclonal anti-Cleaved Caspase-3 (Asp175)	Cell Signaling	Cat#9661; RRID: AB_2341188
Mouse monoclonal anti-Glial Fibrillary Acidic Protein (GFAP)	Millipore	Cat#MAB3402; RRID: AB_94844
Rabbit polyclonal anti-TTC19	Sigma	Cat#HPA023010; RRID: AB_1858429
Mouse monoclonal anti-α-Synuclein Phospho (Ser129)	BioLegend (Covance)	Cat#MMS-5091
Bacterial and Virus Strains		
AAV2/8-TBG-hTTC19^{HIS}	AAV Vector Core TIGEM, Naples, Italy	N/A
Chemicals, Peptides, and Recombinant Proteins		
Dulbecco's Modified Eagle Medium (DMEM)	Invitrogen	Cat#31966-047
Fetal bovine serum (FBS)	Invitrogen	Cat#10270-106
Antibiotic (Penicillin-Streptomycin)	Invitrogen	Cat#15070-063
SILAC DMEM	Thermo Scientific	Cat#89985
Dialyzed FBS	Invitrogen	Cat#26400-044
L-Lysine-$^{13}C_6$,$^{15}N_2$ hydrochloride	Sigma-Aldrich	Cat#608041
L-Arginine-$^{13}C_6$,$^{15}N_4$ hydrochloride	Sigma-Aldrich	Cat#608033
L-Proline	Sigma-Aldrich	Cat#P5607
L-Lysine monohydrochloride	Sigma-Aldrich	Cat#L8662
L-Arginine	Sigma-Aldrich	Cat#A8094
EasyTag L-[^{35}S]-Methionine, 500μCi (18.5MBq), Stabilized Aqueous Solution	PerkinElmer	Cat#NEG709A500UC
n-dodecyl-b-d-maltoside (DDM)	Thermo Scientific	Cat#89903
Digitonin, High Purity	Calbiochem	Cat#300410-5GM
Lipofectamine 2000	Invitrogen	Cat#1168019
Blasticidin	InvivoGen	Cat#ant-bl-1
Hygromycin B	InvivoGen	Cat#ant-hg-5
Doxycyclin hyclate	Sigma	Cat#D9891-1G
Hematoxylin solution according to Mayer	Sigma	Cat#51275-1L
Eosin Y	Sigma	Cat#E4009-25G
Cresyl Violet acetate	Sigma	Cat#C5042-10G
Critical Commercial Assays		
Dako REAL Detection System, Peroxidase/DAB+, Rabbit/Mouse	Dako	Cat#K5001
DeadEnd Colorimetric TUNEL System	Promega	Cat#G7360

(*Continued on next page*)

Continued

REAGENT or RESOURCE	SOURCE	IDENTIFIER
FLUORO-JADE B	Millipore	Cat#AG310-30MG
Amplex Red Hydrogen Peroxide/Peroxidase Assay Kit	Invitrogen	Cat#A22188
TNT T7 Quick Coupled Transcription/Translation System	Promega	Cat#L1170
Experimental Models: Cell Lines		
TTC19 patient skin fibroblasts	Ghezzi et al., 2011	N/A
BCS1L patient skin fibroblasts	Fernandez-Vizarra et al., 2007	N/A
HeLa LYRM7(MZM1L)-HA	Sánchez et al., 2013	N/A
Flp-In T-REx 293 Cell Line	Invitrogen	Cat#R78007
Mouse C57BL/6N embryonic stem (ES) cell Ttc19 recombinant clones	EUCOMM	HEPD0622_3_F12, HEPD0622_3_B10, HEPD0622_3_F09, HEPD0622_3_A11
Experimental Models: Organisms/Strains		
C57BL/6N mice	Charles River Laboratories	http://www.criver.com/files/pdfs/rms/c57bl6/rm_rm_d_c57bl6n_mouse.aspx
Oligonucleotides		
Uqcrfs1-Fw: 5′-TGGTTTGAGCAGCTGTCGCC-3′	Raquel Moreno-Loshuertos (U. Zaragoza, Spain)	N/A
Uqcrfs1-Rv: 5′- AGGCCCTGAGTCCACGTGT-3′	Raquel Moreno-Loshuertos (U. Zaragoza, Spain)	N/A
Uqcrb-Fw: 5′-CGCTTCACTCTCAGGTCAAA-3′	Raquel Moreno-Loshuertos (U. Zaragoza, Spain)	N/A
Uqcrb-Rv: 5′-CCCACAGATCTTAACTAAAAG-3′	Raquel Moreno-Loshuertos (U. Zaragoza, Spain)	N/A
hTTC19-HindIII-Fw: 5′-AAGCTTCACCATGTTCCGGCTCCTGA GCTGG-3′	This work	N/A
hTTC19-WT-Rv: 5′- TATTATTAGAGCTTGACAGAATTTGTCAA AGG-3′	This work	N/A
hTTC19-FLAG-NotI-Rv: 5′-ATGCGGCCGCTTATTACTTATCGTC GTCATCCTT GTAATCGAGCTTGACAGAATTTGTCAAAGG-3′	This work	N/A
hTTC19-6HIS-Rv: 5′-TATTATTAGTGGTGATGGTGATGATGGA GCTTGA CAGAATTTGTCAAAGG-3′	This work	N/A
Recombinant DNA		
pLOX-Ttag-ires-TK	Salmon et al., 2000	Addgene #12246
pSPAX2	Didier Trono	Addgene #12260
pMD2.G	Didier Trono	Addgene #12259
Ptnt	Promega	Cat#L5610; GenBank: AF479322
pCDNA 5/FRT/TO	Invitrogen	Cat#V6520-20
Uqcrfs1/pTNT	Fernández-Vizarra et al., 2010	N/A
Uqcrb/pTNT	This work	N/A
hTTC19/pTNT	This work	N/A
$hTTC19^{6His}$/pTNT	This work	N/A
$hTTC19^{FLAG}$/pCDNA 5/FRT/TO	This work	N/A
Software and Algorithms		
SPSS	IBM	v.19
GraphPad Prism	GraphPad Software	v.5.0a
MaxQuant	Cox and Mann, 2008	http://www.biochem.mpg.de/5111795/maxquant

(*Continued on next page*)

Continued

REAGENT or RESOURCE	SOURCE	IDENTIFIER
Perseus	Tyanova et al., 2016	http://www.biochem.mpg.de/5111810/perseus
Fiji is just ImageJ	Schindelin et al., 2012	https://fiji.sc/
Other		
Pre-cast NuPAGE 4%–12% Bis-Tris gels	Invitrogen	Cat#NP0321BOX; Cat#NP0322BOX; Cat#NP0326BOX
Pre-cast NativePAGE 3%–12% Bis-Tris gels	Invitrogen	Cat#BN2011BX10; Cat#BN2012BX10

CONTACT FOR REAGENT AND RESOURCE SHARING

Further information and requests for resources and reagents should be directed to and will be fulfilled by the Lead Contact, Massimo Zeviani (mdz21@mrc-mbu.cam.ac.uk).

METHOD DETAILS

Cell Culture and Transfection

Human cells were grown in DMEM supplemented with 10% fetal bovine serum, penicillin, and streptomycin in 5% CO_2. For the generation of inducible transgenic TTC19^{FLAG} cell lines, the human cDNA encoding TTC19 plus a C-terminal FLAG (DYKDDDDK) tag was cloned into the pCDNA 5/FRT/TO vector and transfected with Lipofectamine 2000 into Flp-In T-REx human embryonic kidney cells. Following transfection, cells were selected with 15 μg/mL Blasticidin and 100 μg/mL hygromycin B. Gene expression was induced by adding doxycycline to a final concentration of 10 ng/mL for 24 hr.

BNGE

Blue-Native Gel Electrophoresis (BNGE) was performed as described (Nijtmans et al., 2002; Wittig et al., 2006). Mitochondria were solubilized either with n-dodecyl-β-d-maltoside (DDM) 1.6 mg/mg of mitochondrial protein or digitonin 4mg/mg of mitochondrial protein (Wittig et al., 2007). Samples were electrophoresed using pre-cast NativePAGE 3%–12% Bis-Tris gels.

Western Blot

Total cell and tissue lysates were separated by denaturing NuPAGE 4%–12% Bis-Tris gels.

In Organello Import of Radiolabeled Proteins

The import and incorporation into $cIII_2$ of radiolabeled human TTC19, TTC19^{6His}, and mouse Uqcrfs1 and Uqcrb was performed as described (Fernández-Vizarra et al., 2010).

Generation of Ttc19$^{-/-}$ Mice

All procedures were conducted under the UK Animals (Scientific Procedures) Act, 1986, approved by Home Office license (PPL: 7538) and local ethical review. C57BL/6N-A/a targeted ES cells (agouti) were obtained from the EUCOMM consortium. The targeting vector was produced using a KO first allele (reporter-tagged insertion with conditional potential) strategy (Skarnes et al., 2011), with loxP sites surrounding exon 7, encoding the second tetratricopeptide domain, and whose deletion was predicted to lead to no protein expression by non-sense mediated decay. ES cells were injected into C57BL/6N blastocysts, and two 90%–100% chimeric males were obtained. Germline transmission was assessed by backcrossing to C57BL/6N wild-type females and obtained in the 4th litter. The exon cassette was removed by crossing with a general deleter Cre strain. The animals were maintained on a C57BL/6N background. The animals were maintained in a temperature- and humidity-controlled animal-care facility with a 12 hr light/dark cycle and free access to water and food and were sacrificed by cervical dislocation.

Behavioral and Locomotor Analysis

All tests for the assessment of the described parameters were performed according to (Brunetti et al., 2016).

Construction of AAV2/8 Vector

AAV2/8-TBG-hTTC19^{HIS} vector was produced by the AAV Vector Core of the Telethon Institute of Genetics and Medicine (Naples, Italy) by triple transfection of 293T cells and purified by CsCl gradients (Xiao et al., 1999). Physical titers of the viral preparations (genome copies per mL) were determined by real-time PCR (Gao et al., 2000) and dot-blot analysis.

Biochemical Analysis of MRC Complexes

Brain and skeletal muscle samples were snap-frozen in liquid nitrogen and homogenized in 10 mM phosphate buffer (pH 7.4). The spectrophotometric activity of CI, CII, CIII, and CIV, as well as CS, was measured as described, with slight modifications (Kirby et al., 2007).

Morphological Analysis

For histochemical analysis, tissues were frozen isopentane pre-cooled in liquid-nitrogen. Eight μm-thick sections were stained for COX and SDH, as described (Sciacco and Bonilla, 1996). For histological and immunohistochemical analyses, mice were anesthetized with an overdose of pentobarbital and perfused with PBS followed by 4% PFA. Brains were dissected and post fixed in 4% PFA. Whole brains were cut along the sagittal plane and embedded in paraffin. Six μm-thick sections were used for analysis. Hematoxylin-eosin and Nissl staining were performed by standard methods. Immunohistochemistry was performed using specific antibodies against the indicated proteins. TUNEL assay was performed to label apoptotic cells and Fluoro Jade B stain to label degenerating neurons.

ROS Measurement

ROS production in isolated mitochondria without any addition of exogenous substrates (Manczak et al., 2006; Song et al., 2014) was detected by fluorimetric assay using Amplex Red Hydrogen Peroxide/Peroxidase Assay Kit (Invitrogen) according to manufacturer's instructions.

Proteomics

Quantitative mass spectrometry analyses with SILAC were performed as described (Andrews et al., 2013) except that a Q-Exactive+ mass spectrometer (Thermo Fisher) was used in these analyses. Each quantitative comparison was performed in duplicate with reciprocal protein labeling orientations, by growth in media containing heavy and light isotopically labeled arginine and lysine residues. Complexome analysis of samples excised from Blue Native gels was carried out according to (Heide et al., 2012).

Statistical Analysis

All numerical data are expressed as mean ± SEM. After assessment for normality Student's unpaired two-tail t test was used for statistical analysis. Differences were considered statistically significant for $p \leq 0.05$.